

# Doped ZnS:Mn nanoparticles obtained by sonochemical synthesis

O A Korotchenkov<sup>1,4</sup>, A Cantarero<sup>1</sup>, A P Shpak<sup>2</sup>, Yu A Kunitskii<sup>2</sup>,  
A I Senkevich<sup>2</sup>, M O Borovoy<sup>3</sup> and A B Nadtochii<sup>3,5</sup>

<sup>1</sup> Materials Science Institute, Universitat de València, PO Box 22085, E-46071 València, Spain

<sup>2</sup> Kurdyumov Institute of Metal Physics, National Academy of Sciences of Ukraine, Kiev 03680, Ukraine

<sup>3</sup> Department of Physics, T Shevchenko National University of Kiev, Kiev 03680, Ukraine

Received 4 May 2005, in final form 17 June 2005

Published 3 August 2005

Online at [stacks.iop.org/Nano/16/2033](http://stacks.iop.org/Nano/16/2033)

## Abstract

A study of sonochemically synthesized ZnS:Mn nanoparticles is presented. The particles prepared at low rf power (about 20 W) and room temperature coalesce to form morphologically amorphous large species (30–100 nm in diameter). As the power is increased in the range from 20 to 70 W, and the solution temperature is raised to 60 to 80 °C, finer particles are produced with the size ranging from 2 to 20 nm and improved crystallinity. The results indicate the dispersion of the Mn<sup>2+</sup> ions at near-surface sites in the particles. It is shown that the sonochemically fabricated particles approach the quality of the ones obtained by a standard chemical route and show a reasonable luminescence performance.

## 1. Introduction

In the recent past, there has been increased interest in examining the novel and unusual behaviour of doped semiconductor nanoparticles, particularly of ZnS:Mn<sup>2+</sup>, which is commercially used as a phosphor [1] and also in thin-film electroluminescent devices [2]. Due to high luminescence efficiency and excellent luminescent performance [2–6] of nanometre-sized ZnS:Mn<sup>2+</sup>, extensive efforts have been made to produce this material by cost-effective fabrication techniques [4, 7–9].

Quite recently, a simple and inexpensive sonochemical synthesis of nanomaterials was proposed, stimulating intense research efforts, which proved that the technique offers an attractive alternative for the fabrication of nanoscale crystalline and amorphous structures [10]. In particular, studies on the formation of metallosulfides, such as CdS nanoparticles [11, 12], PbS nanorods [13], Sb<sub>2</sub>S<sub>3</sub> microcrystallites [14] and some other related materials [15–17] were conducted.

It is widely recognized that acoustic cavitation provides the primary mechanism for sonochemical effects. Cavitation

serves as a means of concentrating the ultrasonic energy into a localized spot where high temperatures, high pressures and very short lifetimes are achieved [10]. As a consequence, unusual materials can be produced from dissolved precursors. In liquid–solid slurries, cavitation still occurs, and high-velocity interparticle collisions are generated. The particle velocity can be high enough to induce, depending on the collision angle, effective melting at the point of collision or mechanical removal of a surface material. These unique conditions can be beneficial to rearrangements of the host atoms and dopants both on the surface and in the bulk of nanoparticles. The importance of the spatial distribution of dopants has been widely addressed, e.g., for Mn<sup>2+</sup>-doped ZnS nanoparticles [3–6, 18, 19]. Mn<sup>2+</sup> ion d electrons act as efficient luminescent states which interact strongly with s–p electronic states of the host material into which the external excitation is usually directed. The spatial overlap of the host and dopant states, which varies with their distributions, influences the luminescence performance of the particles. This is important because sensors, displays and light-emitting devices utilizing ZnS:Mn nanoparticles can be better performing due to rapid energy transfer to the Mn<sup>2+</sup> ions and fast recombination with the Mn<sup>2+</sup> colour centre.

Therefore, an intense local heating that results in high-velocity interparticle collisions is thought to be capable of inducing striking changes in the dopant distribution in the

<sup>4</sup> Permanent address: Department of Physics, T Shevchenko National University of Kiev, Kiev 03680, Ukraine.

<sup>5</sup> Present address: Department of Physics and Astronomy, University of Mississippi, University, MS 38677, USA.

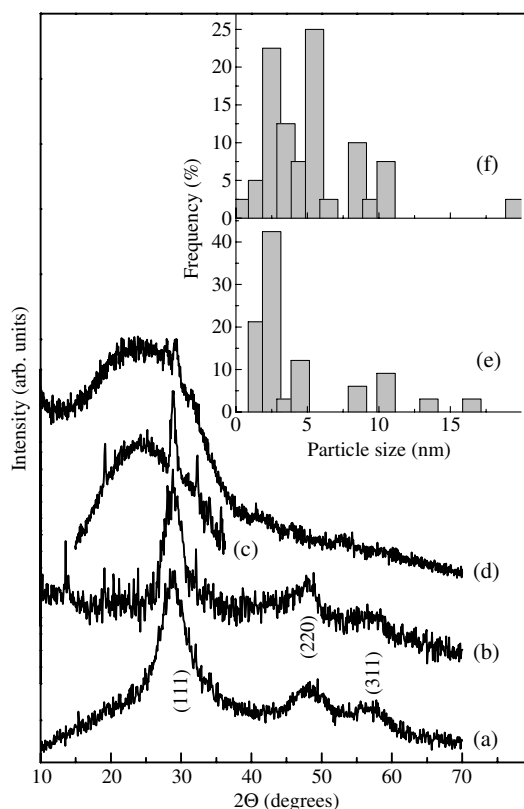


**Figure 1.** XRD patterns of ZnS:Mn particles: (a) CH, (b) SCH sample 1, (c) SCH sample 2 and (d) SCH sample 3. Histograms (e) and (f) show the size distributions of the particles in figures 2(a) and (b), respectively.

sonochemically fabricated material. This is, for example, due to the fact that  $\text{Mn}^{2+}$  ions can effectively diffuse into the ZnS lattice at elevated temperatures [20]. Especially for the surface composition, the consequences of the sonochemical routes of doping can be quite substantial. Despite the advance of sonochemical techniques, the doping of semiconductor nanoparticles promoting their luminescence has not yet been achieved. Here, we report the synthesis of ZnS:Mn nanoparticles by a sonochemical reaction, the optoelectronic properties of which can be of potential utility.

## 2. Experimental details

The particles were prepared by using the reaction between zinc and sulfur ions released into the solution. Thiourea was used as  $\text{S}^{2+}$  source whereas either  $\text{ZnSO}_4$  or  $\text{ZnCl}_2$  was used as  $\text{Zn}^{2+}$  source. The results reported below were obtained with zinc sulfate. In a typical procedure, 4 g of  $\text{ZnSO}_4$  and 1.8 g of thiourea were dissolved in 100 ml of distilled water, yielding  $[\text{Zn}] \approx [\text{S}] \approx 0.1$  M. Doping was achieved by the addition of 0.21 g  $\text{MnSO}_4$  to the solution, yielding Mn concentration of about 5 mol% relative to Zn. All chemicals were analytic grade and were used without further purification.

Sonication of the above solution was performed using a model 450 Branson sonifier (0.5 inch in diameter, direct-immersion Ti tip) operated in continuous mode at 20 kHz

and with a power ( $P$ ) output level ranging from 20 to 70 W. The tip was dipped into a cylindrical jacketed cooling flask of about 5 cm in internal diameter. The temperature ( $t$ ) of the bulk solution was kept constant between 20 and 80 °C during the entire treatment by using a cooling recirculator. The sonication time was varied from 3 to 20 h. For long times, a special externally driven cell was designed in order to avoid the contamination of the solution by the tip metal particles.

The sonication resulted in a white cloudy solution. The product obtained was recovered by centrifugation (10 000 rpm, 30 min), exhaustively washed three times with distilled water for removal of by-products, and air-dried overnight. Experimental samples were formed by grinding the collected products into powders.

In this work, the properties of sonochemically (SCH) fabricated particles were compared with those of ZnS:Mn nanoparticles prepared by a chemical (CH) process described, e.g., by Igarashi *et al* [21], without the modification by acrylic acid. The Mn concentration during the chemical and sonochemical synthesis was kept at approximately the same level. For the purposes of comparison, undoped ZnS particles fabricated by SCH reaction at  $t = 80$  °C,  $P = 70$  W were also produced.

Particle size and crystalline phase were determined by an x-ray powder diffraction (XRD) technique using a Seifert XRD 3003TT diffractometer with Cu  $K\alpha$  radiation at  $\lambda = 1.54$  Å. The morphology of the grown product was checked by taking scanning electron microscopy (SEM) images recorded with a Hitachi S-4100 microscope. The powdered samples were dispersed in acetone by sonication, dropped onto an aluminium substrate and covered with a sputtered gold layer. A JEOL JEM-1010 transmission electron microscope (TEM) was also used to estimate the particle size. The samples used for TEM observations were prepared by dispersing the synthesized powders in acetone followed by a 1 h treatment in an ultrasonic cleaning bath. Then a drop of the solution was placed on a holey carbon-covered copper grid, dried and placed in the microscope. X-band electron paramagnetic resonance (EPR) spectra were collected on a Radiopan PE1304 spectrometer. X-ray photoelectron spectroscopy (XPS) was carried out on a series 800XPS Kratos analytical instrument using nonmonochromatic Al  $K\alpha$  x-rays at 1486.6 eV as the excitation source and choosing C 1s (285.0 eV) as the reference line. Photoluminescence (PL) spectra were taken on a SPEX-1680 monochromator using the 325 nm line of a He–Cd laser as the excitation source. All the experiments presented here were performed at room temperature.

## 3. Results and discussion

The XRD patterns shown in figures 1(a) and (b) demonstrate that both the SCH and CH particles have the sphalerite structure and match the Bragg angles for (111), (220), and (311) planes of ZnS. Using the Debye–Scherrer equation [22], from the full width at half maximum (FWHM) of the (111) peaks the average sizes of these particles are 2.2 (CH) and 2.9 (SCH) nm. TEM images of the same samples are displayed in figures 2(a) and (b); histograms (e) and (f) in figure 1 show the size distribution of the particles in the images. Statistically averaging on several TEM images, the mean particle size is estimated to be

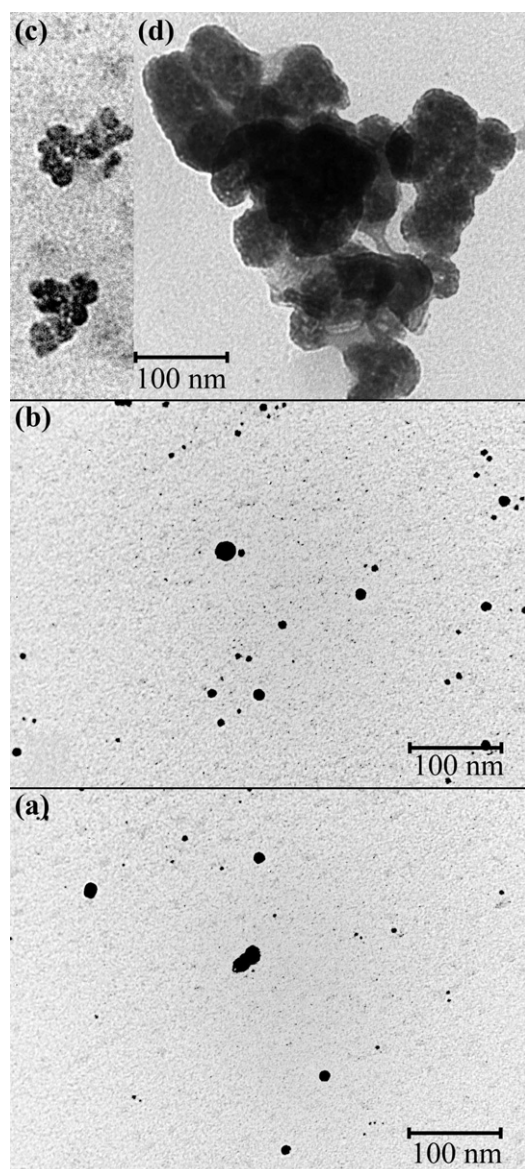


**Figure 2.** TEM images of ZnS:Mn particles: (a) CH, (b) SCH sample 1, (c) SCH sample 2 and (d) SCH sample 3.

( $3.7 \pm 1.5$ ) and ( $6.5 \pm 3.5$ ) nm for the CH and SCH particles, respectively. Comparison of the particle size determined from TEM to that determined from XRD demonstrates a good correspondence, suggesting that the prepared particles are mostly single-domain crystallites.

However, the size, crystallinity and morphology of the particles depend on the sonication parameters (e.g., power and solution temperature). This is seen by comparing XRD patterns (b), (c) and (d) in figure 1 taken in the powders obtained at  $t = 80^\circ\text{C}$ ,  $P = 70$  W (sample 1),  $t = 60^\circ\text{C}$ ,  $P = 50$  W (sample 2), and  $t = 20^\circ\text{C}$ ,  $P = 20$  W (sample 3), respectively. It is seen that, upon decreasing  $P$  and  $t$ , the broad peak at  $2\theta \approx 25^\circ$  evolves, indicating the growth of disordered contributions in the resulting product. Next, the (111) diffraction peak sharpens in (c), indicating the increased particle size (9.6 nm), and finally merges in the broad halo in pattern (d). Since the crystalline contributions are washed out

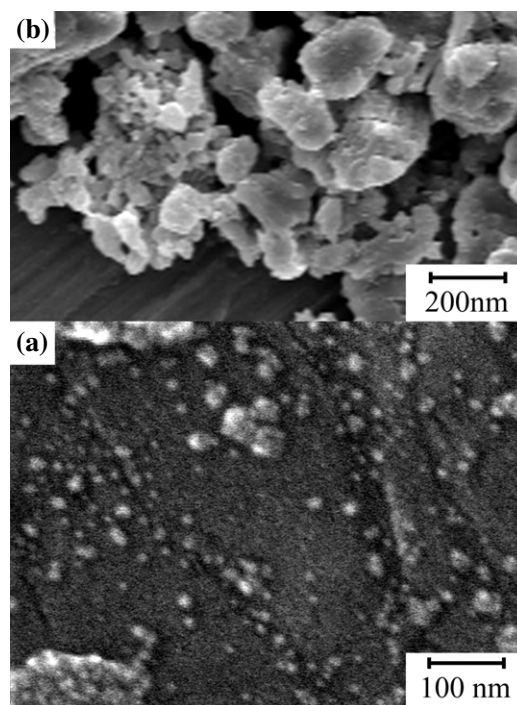


**Figure 3.** SEM images of the grown product composed of sample 1 (a) and sample 3 (b) particles.

in (d) this suggests that sample 3 is mostly amorphous-like. TEM images (c) and (d) in figure 2 show the increased particle size,  $\geq 15$  nm in (c) and in the range from 30 to 100 nm in (d).

From the SEM images of the as-grown material shown in figure 3, a large number of aggregated particles are evident. The sample 3 particles exhibited in panel (b) are characterized by quite rough surfaces and the presence of connection necks between the particles with various sizes. Although some nanoparticles are most likely lost in the wash cycles, small particles which are less than 10–15 nm in diameter are present in sample 1, as evidenced by panel (a) in figure 3. Nevertheless, larger species varying from 40 to 170 nm in size also occur in figure 3(a), which are probably due to aggregated particles whose size is most closely reflected in the XRD data in figure 1. Furthermore, it may be suggested that aggregated nanoparticles are in part re-suspended due to the preparation of particles for TEM, so that the individual nanoparticles are resolved in figures 2(a) and (b). Below, because of the pure crystallinity of sample 3, only SCH samples 1 and 2 are mainly compared with the CH sample. Close-up XRD, TEM and XPS data were also obtained in the undoped SCH sample, but these are not shown here since they do not add significant information.

Figure 4 displays the EPR spectra of the powders. Two distinct signals can be distinguished from the spectra: hyperfine structured  $\text{Mn}^{2+}$  lines present in all the spectra, and a broad background signal, increasing in intensity from (a) to (c). The background signal is reminiscent of the one broadened in exchange interaction of the  $\text{Mn}^{2+}$  ions [23–25]. Obviously, this should increase in intensity upon increasing of the particle size [25]. Therefore, the observed evolution of the background signal is consistent with the particle sizes deduced from



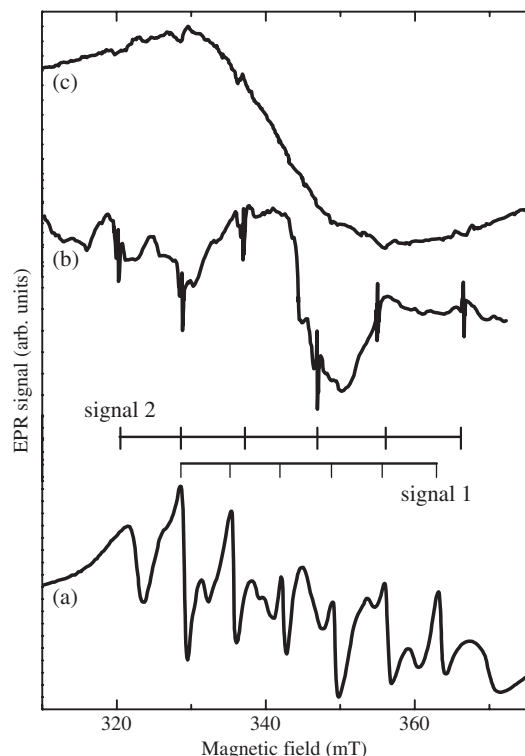


**Figure 4.** EPR spectra of ZnS:Mn particles: (a) CH, (b) SCH sample 1 and (c) SCH sample 2.

figures 1 and 2. The dominance of this signal in spectrum (c) of figure 4 is furthermore consistent with the enhanced disorder contributions revealed by the occurrence of a broad halo in figure 1(c). Indeed, the six-line, poorly resolved spectrum is known to arise in dilute environments [26]. Importantly, the hyperfine structure lines grouped in signal 2 in figure 4 are observed in all the samples, although they are suppressed in spectrum (c) and seen only as a weak spectrum superposed on the broad background signal. In marked contrast, the other sextet signal marked signal 1 is only detected in CH particles. It is believed that signal 1 arises in the interior while signal 2 is attributed to the  $\text{Mn}^{2+}$  ion near the particle surface [21, 23]. Thus, it is likely that the quenching of signal 1 in spectra (b) and (c) of figure 4 is indicative of the dispersion of the  $\text{Mn}^{2+}$  ions at near-surface sites in SCH particles.

In figure 5, the XPS survey spectra are displayed, and detailed scans of the Zn 2p and Mn 2p regions are shown in figure 6. Numerous photoemission and Auger peaks feature the survey spectra, the most prominent of which are labelled. There are three relevant points. First, the Mn:Zn ratio is found to be 0.005 (CH), 0.077 (SCH sample 1) and 0.017 (SCH sample 2). Since XPS is a rather surface-sensitive technique, the XPS spectra can primarily reveal the chemical state of the outermost layers of the particles and the enhanced ratio of the Mn 2p to Zn 2p peaks in SCH particles is just the type of behaviour which would be expected from the near-surface location of the  $\text{Mn}^{2+}$  ions.

Second, by comparison of the ratio of the XPS intensities of the Zn 2p and S 2p peaks, SCH particles have a larger amount of Zn on the surface compared to that in CH particles. Thus, the Zn:S ratios are 1.6 and 2.1 in the CH and SCH (sample 1)

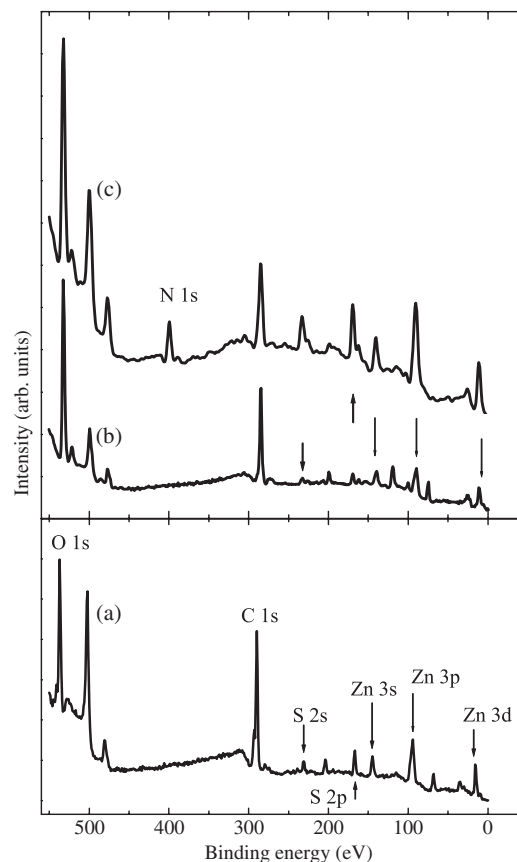


**Figure 5.** XPS survey spectra of ZnS:Mn CH (a), SCH sample 1 (b) and sample 2 (c) particles.

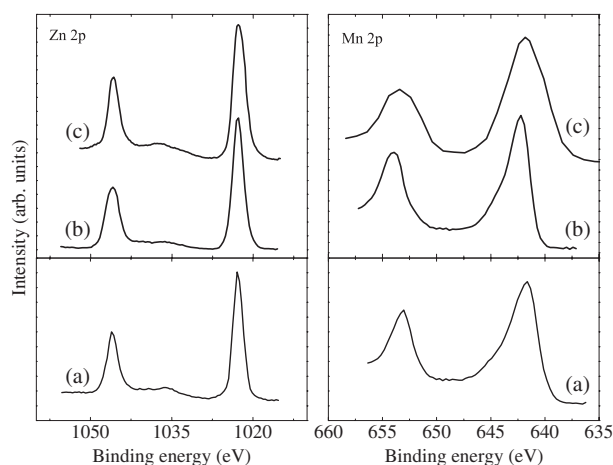


**Figure 6.** XPS detail scans in Mn 2p (right panel) and Zn 2p (left panel) regions. (a)–(c) The same as in figure 5. The spectra are scaled arbitrarily whereas accurate atomic ratios of Mn:Zn (see text) were obtained by integrating the peak area for both the lines and dividing by the atomic sensitivity factors [31].

particles, respectively. The undoped SCH particles show the ratio of 3.0. It is known that  $\text{Mn}^{2+}$  can substitute for  $\text{Zn}^{2+}$  ions in the crystal lattice of ZnS because of their close ionic radii (0.80 and 0.83 Å for  $\text{Mn}^{2+}$  and  $\text{Zn}^{2+}$ , respectively). As the Zn 2p peak in SCH ZnS particles appears more intense than in SCH ZnS:Mn and the one in SCH ZnS:Mn turns out to appear

more intense than in CH ZnS:Mn, these might be due to the facts that (i) the surface of SCH particles is terminated by Zn to a greater extent than the CH particle surface and (ii) Mn ions enrich the surface of the SCH ZnS:Mn particles by substituting Zn ions.

Also, the N 1s signal is seen in spectrum (c) of figure 5 whereas it is absent in spectra (a) and (b). This indicates that some N-containing groups are present in sample 2. There are at least two plausible pathways for their formation. First, thiourea forms stable complexes with  $\text{Zn}^{2+}$  and  $\text{Mn}^{2+}$ , i.e.  $[(\text{Zn}, \text{Mn})(\text{SC}(\text{NH}_2)_2)_2]$  [27]. The subsequent decomposition of the complex compounds at suitable temperature and pressure achieved near the collapsed bubble leads to the formation of ZnS:Mn. Whilst it can be suggested that complex may be left in the resulting powder, this seems unlikely since the complexes of thiourea with metal ions are easily soluble in water and should be removed from the product. Second, most reports [28–30] have concluded that thiourea is readily oxidized in aqueous solutions to form  $(\text{NH}_2)_2(\text{NH})_2\text{C}_2\text{S}_2$ . It is expected that this product can decompose to CN-containing groups arising from  $\text{NCNH}_2$ . Noticeably, another product of the decomposition is sulfur [29]. This fact may be consistent with the increased relative intensity of the sulfur lines in figure 5(c). Nevertheless, further experiments are needed in order to clarify the nature of the groups. At this point, it is likely that N-containing groups introduce an enhanced disorder in the sample 2 particles, and this result is consistent with the XRD and EPR data.

The PL spectra of the particles are presented in figure 7. Spectra (a) and (b) are dominated by the  $\text{Mn}^{2+}$  ion yellow emission at about 600 nm. Noticeably, their line shapes are almost identical but the peak in spectrum (b) is red-shifted ( $\approx 9$  nm) compared to that in spectrum (a). This result may be consistent with the models involving either a size-dependent phonon coupling [25] and crystal fields [32], or a near-surface location of the  $\text{Mn}^{2+}$  ions [33] as an explanation for the PL peak shift. From PL spectra acquired in repeatedly produced SCH samples, the peak position of the yellow emission undergoes a red shift with increasing particle size up to about 7 nm; see figure 8. When the size is increased above  $\approx 8$  nm, the position goes to lower wavelengths. Explaining this observation, it should be pointed out that the  $\text{Mn}^{2+}$  emission band in ZnS nanoparticles may shift to higher or to lower energies compared to bulk ZnS:Mn, depending on both the size and the surface effects [25]. Therefore, at very small crystalline sizes ( $< 7$  nm) because the density of surface states in SCH particles is reliant upon the sonication parameters, the PL band shifts to lower energies. Larger particles were produced with varying sonication conditions. Hence, the particle crystallinities and morphologies of these SCH products are remarkably different, as illustrated in figures 1–3. This fact may be responsible for the decreasing peak wavelength above  $\approx 8$  nm (figure 8), although the mechanism for this is unclear.

Spectra (b), (c) and (d) in figure 7 show the effects of particle morphology and crystalline phase on the PL line shape. The luminescence intensity decreases from spectrum (b) to spectrum (d) and the shape of the spectral band is remarkably changed. Note that the blue emission peaked at about 440 nm is observed to strengthen in spectrum (c) at the expense of the yellow emission, which is due to prevalence of the zinc vacancy

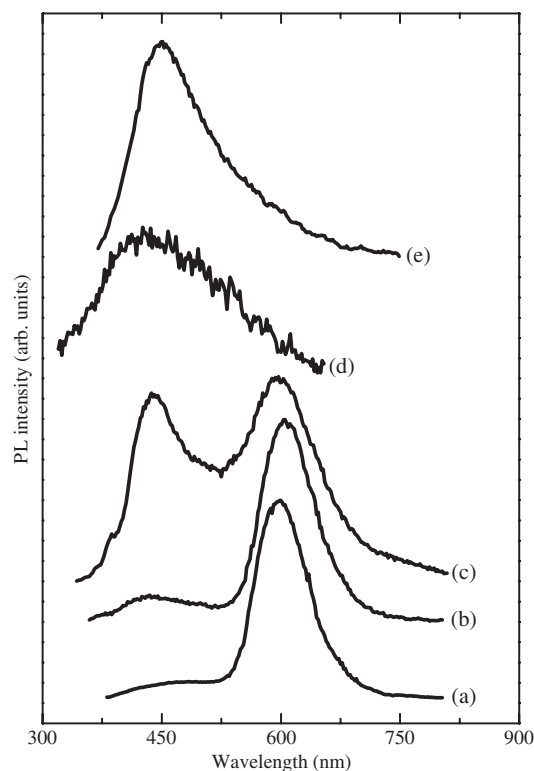


**Figure 7.** Normalized PL spectra of ZnS:Mn particles: (a) CH, (b) SCH sample 1, (c) SCH sample 2, (d) SCH sample 3 and (e) undoped SCH ZnS particles.

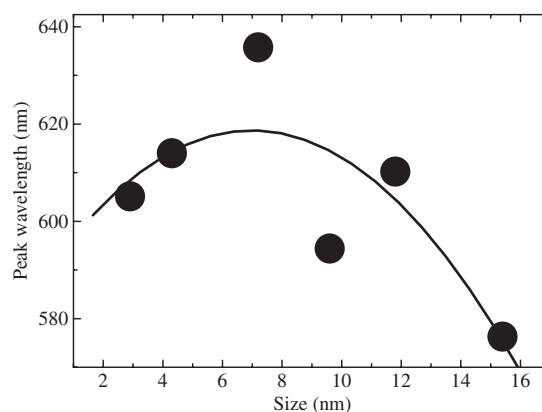


**Figure 8.** Change of the yellow emission peak position upon average size of SCH ZnS:Mn particles determined from the FWHM of the XRD lines. The points are experimental data; the curve is an aid to guide the eye.

centre [34], thus indicating an increased disorder in SCH sample 2. Moreover, SCH sample 3 obtained at the smallest acoustic power and solution temperature shows no significant PL in the yellow band exhibiting a broad blue emission; see spectrum (d) in figure 7. Since spectrum (d) is quite similar to spectrum (e) taken in the undoped ZnS particles, this indicates that  $\text{Mn}^{2+}$  centres are not activated in SCH sample 3. Therefore, it may be suggested that the elevated local temperatures in the sonicated solution that promote improved crystallinity of the resulting SCH product also cause  $\text{Mn}^{2+}$  diffusion inside ZnS particles.

On the assumption that the  $\text{Mn}^{2+}$  ions predominantly reside in the lattice sites beneath the particle surface in SCH samples 1 and 2 while they are located on the surface outside and deep inside the SCH sample 3 and CH particles, respectively, spectra (a)–(d) in figure 7 show the line shapes characteristic of the  $\text{Mn}^{2+}$  inside versus  $\text{Mn}^{2+}$  outside locations. Indeed, earlier results [4] have given evidence that, if the  $\text{Mn}^{2+}$  ions on the outside diffuse into the nanocrystallite, the yellow emission is expected to appear. Instead, the addition of  $\text{Mn}^{2+}$  to the outside of preformed ZnS nanoparticles suppresses the yellow emission and promotes the near-band-gap ultraviolet emission peaked at about 350 nm. Consistent with this conclusion, the ultraviolet emission is totally absent in spectrum (a) while a weakly resolved emission is seen to arise below  $\approx 380$  nm in spectra (b) and (c), probably indicating the near-surface location of the  $\text{Mn}^{2+}$  ions in SCH sample 1 and 2. On the other hand, the subsidiary emission on the high-energy side of the blue emission band (at wavelengths  $\leq 370$  nm) is relatively enhanced in spectrum (d) with no yellow band observed, supporting the above assumption on the  $\text{Mn}^{2+}$  outside location in SCH sample 3.

It should be mentioned that photoluminescence of SCH particles remains significantly less intense (about an order of magnitude) than that of CH particles. However, this is not unexpected, given that previous results have demonstrated that there should likely be a large density of coordination defects on the surfaces of the nanoparticles or some other kind of nonluminescent layer which are thought to act as nonradiative recombination sites [2, 35]. Therefore, it clearly is likely that the near surface location of the  $\text{Mn}^{2+}$  itself is responsible for the PL quenching due to increased nonradiative recombination rate. Hence, a thorough understanding of surface effects in SCH particles will be essential if this technology is to be successfully exploited to produce high-performance phosphor materials.

#### 4. Conclusions

In summary, we have produced Mn-doped ZnS nanoparticles by a sonochemical method. Their x-ray diffraction patterns, morphologies, chemical contents and photoluminescence lineshapes are of comparable quality to the ones taken in chemically synthesized ZnS:Mn nanoparticles. These observations in total argue the suggestion that the  $\text{Mn}^{2+}$  ions are predominantly located near the surface of sonochemically fabricated nanoparticles, which may be very important for possible nanoelectronics applications. We are then led to hypothesize, provisionally, that optimizing the surface capping layer of the particles would improve their luminescence efficiency.

#### Acknowledgments

We gratefully acknowledge helpful discussions with D Beltrán and J Latorre. OAK thanks the Ministerio de Educación, Cultura y Deporte of Spain for financial support.

#### References

- [1] Shionoya S and Yen W M 1999 *Phosphor Handbook* (Boca Raton, FL: CRC Press)
- [2] Dinsmore A D, Hsu D S, Gray H F, Qadri S B, Tian Y and Ratna B R 1999 *Appl. Phys. Lett.* **75** 802
- [3] Bhargava R N, Gallagher D, Hong X and Nurmikko A 1994 *Phys. Rev. Lett.* **72** 416
- [4] Sooklal K, Cullum B S, Angel S M and Murphy C J 1996 *J. Phys. Chem.* **100** 4551
- [5] Smith B A, Zhang J Z, Joly A and Liu J 2000 *Phys. Rev. B* **62** 2021
- [6] Bol A A and Meijerink A 2001 *J. Phys. Chem. B* **105** 10197
- [7] Yu I, Isobe T and Senna M 1996 *J. Phys. Chem. Solids* **57** 373
- [8] Gan L M, Liu B, Chew C H, Xu S J, Chua S J, Loy G L and Xu G Q 1997 *Langmuir* **13** 6427
- [9] Cao L, Zhang J, Ren S and Huang S 2002 *Appl. Phys. Lett.* **80** 4300
- [10] Suslick K S and Price G J 1999 *Annu. Rev. Mater. Sci.* **29** 295
- [11] Sostaric J Z, Caruso-Hobson R A, Mulvaney P and Grieser F 1997 *J. Chem. Soc. Faraday Trans.* **93** 1791
- [12] Dhas N A and Gedanken A 1998 *Appl. Phys. Lett.* **72** 2514
- [13] Zhou S M, Feng Y S and Zhang L D 2003 *J. Mater. Res.* **18** 1188
- [14] Zhang J H, Chen Z, Wang Z L and Ming N B 2003 *J. Mater. Res.* **18** 804
- [15] Gedanken A, Reisfeld R, Sominski L, Zhong Z, Koltypin Yu, Panczer G, Gaft M and Minti H 2000 *Appl. Phys. Lett.* **77** 945
- [16] Lee S, Han I-K and Cho W-J 2003 *Proc. SPIE Int. Soc. Opt. Eng.* **5224** 176
- [17] Kumar R V, Mastai Y, Diamant Y and Gedanken A 2001 *J. Mater. Chem.* **11** 1209
- [18] Bhargava R N, Gallagher D and Welker T 1994 *J. Lumin.* **60/61** 275
- [19] Bol A A and Meijerink A 1998 *Phys. Rev. B* **58** R15997
- [20] Yu I, Isobe T and Senna M 1996 *J. Phys. Chem. Solids* **57** 373
- [21] Igarashi T, Isobe T and Senna M 1997 *Phys. Rev. B* **56** 6444
- [22] Cullity D B 1978 *Elements of X-ray Diffraction* (Reading, MA: Addison-Wesley)
- [23] Kennedy T A, Glaser E R, Klein P B and Bhargava R N 1995 *Phys. Rev. B* **52** R14356
- [24] Counio G, Esnouf S, Gacoin T and Boilot J P 1996 *J. Phys. Chem.* **100** 20021
- [25] Chen W, Sammynaiken R, Huang Y, Malm J-O, Wallenberg R, Bovin J-O, Zwiller V and Kotov N A 2001 *J. Appl. Phys.* **89** 1120
- [26] Griscom D L and Griscom R E 1967 *J. Chem. Phys.* **47** 2711
- [27] Xia B, Lenggoro I W and Okuyama K 2002 *Chem. Mater.* **14** 4969
- [28] Jagminas A, Niaura G, Judzentiene A and Juskenas R 2004 *Appl. Surf. Sci.* **239** 72
- [29] Ratajczak H M, Pajdowski L and Ostern M 1975 *Electrochim. Acta* **20** 431
- [30] Szymaszek A, Biernat J and Pajdowski L 1977 *Electrochim. Acta* **22** 359
- [31] Wagner C D, Riggs W M, Davis L E, Moulder J F and Muilenberg G E 1979 *Handbook of X-ray Photoelectron Spectroscopy* (Eden Prairie, MN: Perkin Elmer)
- [32] Yang H, Holloway P H and Ratna B R 2003 *J. Appl. Phys.* **93** 586
- [33] Chen W, Joly A G and Zhang J Z 2001 *Phys. Rev. B* **64** 0412021
- [34] Samelson H and Lempicki A 1962 *Phys. Rev.* **125** 901
- [35] Chen L, Zhang J, Luo Y, Lu S and Wang X 2004 *Appl. Phys. Lett.* **84** 112